

Article

# Research on Azimuth DBF Method of HRWS SPC MAB SAR Imaging Mode with Non-Ideal Antenna Mode

**Weihua Zuo \***  **Caipin Li, Sheng Zhang, Dongtao Li, Wencan Peng, Jinwei Li, Dong You and Chongdi Duan**

Xi'an Branch of China Academy of Space Technology, Xi'an 710100, China; licp@cast504.com (C.L.); zhongs18@cast504.com (S.Z.); lidt@cast504.com (D.L.); pengwc@cast504.com (W.P.); lijw@cast504.com (J.L.); youd@cast504.com (D.Y.); duancd@cast504.com (C.D.)

\* Correspondence: zuowh@cast504.com

**Abstract:** Single-phase center multiple azimuth beam (SPC MAB) mode is an effective method for high-resolution wide-swath (HRWS) SAR imaging. The traditional azimuth spectrum reconstruction method for SPC MAB mode is based on the combination scheme from which fake targets along the azimuth direction arise because the inter-beam interference is not considered. When the real antenna mode is inconsistent with the ideal one, the disadvantages of the combination scheme become more serious. In this paper, based on the basic theory of the low-pass, band-limited, multiple-channel under-sampling and reconstruction, a novel digital beam-forming method is proposed for the SPC MAB imaging mode with ideal antenna mode first. The method analyzes the system functions of the sub-beams, based on which digital beam-forming filters are designed for all the sub-beams. The designed filters can reconstruct the correct wide-bandwidth azimuth spectrum and suppress the inter-beam interference simultaneously. Furthermore, the proposed method is extended to SPC MAB mode with the non-ideal antenna mode. The simulation experiments prove the validities of the proposed method both for azimuth spectral reconstruction and the inter-beams interfering suppressing, no matter that the SPC MAB's antenna mode is ideal or non-ideal.



**Citation:** Zuo, W.; Li, C.; Zhang, S.; Li, D.; Peng, W.; Li, J.; You, D.; Duan, C. Research on Azimuth DBF Method of HRWS SPC MAB SAR Imaging Mode with Non-Ideal Antenna Mode. *Remote Sens.* **2024**, *16*, 1552. <https://doi.org/10.3390/rs16091552>

Academic Editor: Massimiliano Pieraccini

Received: 13 March 2024

Revised: 19 April 2024

Accepted: 24 April 2024

Published: 26 April 2024



**Copyright:** © 2024 by the authors. Licensee MDPI, Basel, Switzerland. This article is an open access article distributed under the terms and conditions of the Creative Commons Attribution (CC BY) license (<https://creativecommons.org/licenses/by/4.0/>).

## 1. Introduction

High-resolution wide-swath (HRWS) space-borne synthetic aperture radar (SAR) is important research filed in the remote sensing community during the recent decades. The traditional SAR imaging modes, such as spotlight, side-looking and the scan mode, cannot fulfill wide-swath coverage and high azimuth resolution simultaneously because of their contradicting requirements on pulse repetition frequency (PRF). In order to conquer this inherent limitation, several imaging modes have been innovated since the 1980s. A. Currie proposed the multiple elevation beam (MEB), displaced phase center multiple azimuth beam (DPC MAB) and single-phase center multiple azimuth beam (SPC MAB) [1]. In the DPC MAB mode, multiple identical antennas are displaced along the azimuth direction. One of these antennas transmits the radar signal, and all the antennas receive the backscattered echoes at different azimuth positions simultaneously. Then, the required PRF can be decreased by  $N_a$  times ( $N_a$  is the azimuth antennas' number) because of the additional samplings and because the pulse repetition interval (PRI) is much longer for receiving wide-swath echoes. In the SPC MAB mode, a wide azimuth beam transmits the radar signal, and multiple azimuth narrow beams receive the echoes, as shown in Figure 1. The required PRF needs to be just larger than the Doppler bandwidth of the narrow beams. The decreased PRF can fulfill the wide-swath imaging. From the previous analysis, it can be found that, in the DPC MAB and SPC MAB modes, the PRF can be decreased by  $N_a$ ; thus, the wide swath can be fulfilled. The difference between these two imaging modes lies

in the azimuth high-resolution fulfilling mechanism. In DPC MAB, the azimuth channels' signals are all under-sampled because the transmitting and the receiving antennas cover the same Doppler bandwidth. The aliased sub-beam Doppler bandwidth must be utilized to recover the wide Doppler bandwidth for high azimuth resolution imaging. In SPC MAB, the transmitting Doppler bandwidth is  $N_a$  times larger than that of the receiving sub-beams. In fact, the receiving sub-beams are well-sampled. Intuitively, they can be combined to obtain the high azimuth resolution. The DPC and SPC MAB modes can effectively solve the previous mentioned limitation, but some new problems emerge, such as the inter-beam interference in elevation or azimuth [2], which deteriorates the two-dimensional imaging qualities. Based on these imaging modes, improved schemes were proposed. The sweep SAR and the scan on receiver (SCORE) SAR [3] can reduce the system power requirement and improve the imaging qualities along the elevation direction. The multi-dimensional waveform encoding technology [4,5] and the digital beam forming (DBF) technology [6] can improve the two-dimensional imaging qualities. The DPC MAB technologies with TOPSAR or scan SAR can obtain ultra-HRWS imaging abilities [7,8]. In recent years, the staggered SAR was proposed based on the reflector antenna configuration to reduce the antenna size and the total weight of the payload [9–12]. The multi-input, multi-output (MIMO) SAR was also used to solve the HRWS inherent problems [13,14]. The corresponding processing algorithms were researched [15,16]. Some airborne experiments based on the previous technologies were carried out [17–20]. At present, the HRWS SAR satellites with reflector antennas based on the SPC MAB, sweep and staggered SAR technology, i.e., NISAR and tandem-L, are in the development stage [21,22]. The launch of all these satellites is sought for approximately 2024. The HRWS SAR satellites with phase array antennas based on the DPC MAB mode, i.e., LT-1, 2, are already launched [23–25].

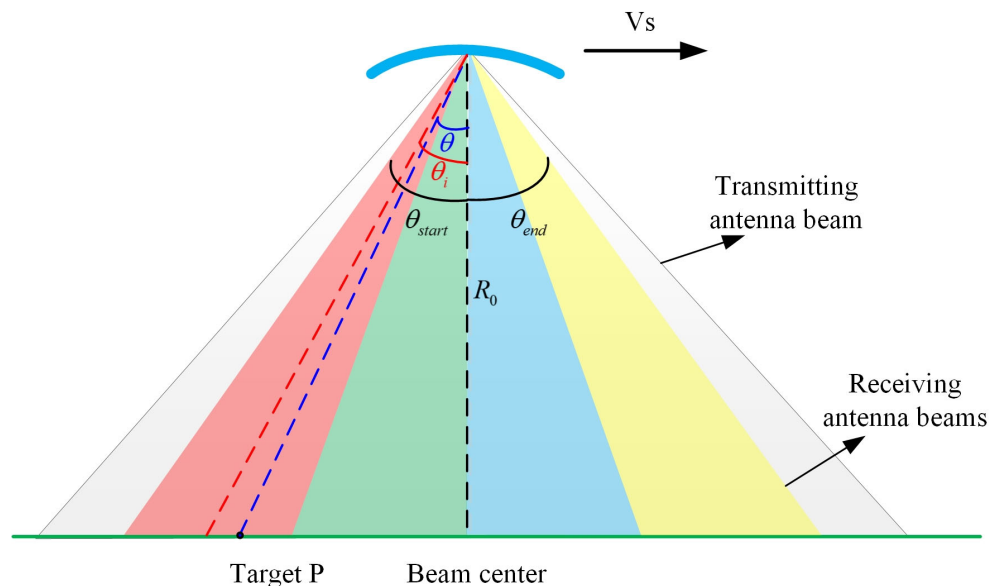


**Figure 1.** Antenna modes for SPC MAB.

According to the previous analysis, it is found that the SPC MAB mode with a reflector antenna is a widely accepted candidate for HRWS imaging. Its azimuth antenna configurations are shown in Figure 1, in which the thick blue curve represents the reflector; the gray area represents the transmitting wide beam; the red, green, blue and yellow areas represent the azimuth receiving sub-beams;  $V_s$  is the velocity of the satellite;  $\theta_{start}$  and  $\theta_{end}$  are the targets' azimuth observation start and end squint angle, respectively;  $R_0$  is the targets' shortest slant range;  $\theta_i$  is the squint angle of the  $i$ th ( $i = 1, \dots, 4$  in this example) azimuth sub-beam; and  $\theta$  is the azimuth look angle of point target P. In the SPC MAB mode, the azimuth transmitting beam is  $N_a$  times wider than that of the receiving beam. In order to obtain high azimuth resolution, the total Doppler band should be reconstructed from

that of the sub-beams. The traditional and simple method is based on the combination scheme [26,27], i.e., all the sub-beam Doppler bands are shifted to their own Doppler frequency centers and combined to form a wide-bandwidth azimuth signal. However, this method does not consider the inter-beam interference; thus, “ghost” targets appear along the azimuth direction in the final focused image. Although this phenomenon can be reduced or removed through the side-lobe depression to all sub-beams, this method would add dramatic complexities to the antenna system, which cannot be accepted by the HRWS satellites with a limited payload space and weight envelop. In the literature [27,28], the azimuth DBF methods based on the space–time adaptive processing (STAP) theory are researched to deal with the inter-beam interference problem. These methods can depress the interference effectively, and the total azimuth Doppler spectrum can be reconstructed perfectly. But these methods are based on the ideal antenna modes. When a reflector antenna is employed in the SAR system, in fact, the real transmitting and receiving antenna modes are quite different from the ideal ones, which means, if the proposed methods in [27,28] were used to handle the real raw data directly, the mismatch between the ideal and the real antenna patterns would make the inter-beam interference depressing, and the azimuth spectrum reconstruction would become invalid.

In this paper, based on the theory of the low-pass, band-limited, multiple-channel under-sampling and reconstruction [29], a novel azimuth DBF method is proposed for the SPC MAB mode with, first, the ideal antenna mode. Then, this method is extended to deal with the non-ideal antenna pattern situation. Much different from the method proposed in the literature [15,27,28], in our method, the sub-beam signals are regarded as under-sample versions of the total azimuth signal weighted by different system transmission functions [30]. The system transmission function of each sub-beam is determined by the corresponding transmitting and receiving antenna mode. According to the transmission functions, the reconstruction filters for all the sub-beams can be designed. After being processed by the designed filters, the output signals of all the sub-beams are combined to obtain the correct total azimuth signal, and the inter-beam interference can be suppressed simultaneously.

This paper is organized as follows. In Section 2, the signal mode of the SPC MAB with a reflector antenna is established. Section 3 analyzes the transmission functions of all the azimuth sub-beams with ideal antenna modes first, and the corresponding reconstruction filters are designed. Then, this method is extended to handle the non-ideal antenna mode situation. Section 4 gives the simulation experiment results. Discussions and conclusions are given in Section 5.

## 2. Signal Mode of SPC MAB with Reflector Antenna

In the SPC MAB mode, the chirp signal is transmitted through an azimuth wide beam as shown in Figure 1 with gray lines. The transmitting signal is as Equation (1), in which  $\tau = t - \eta = t - mPRI$  is the fast time variable,  $T_p$  is the pulse duration time, and  $f_c$  is the carry frequency. Within the  $\tau$  expression,  $PRI$  is the transmitting pulse period interval,  $m$  represents the  $m$ th transmitting pulse, and  $\eta = mPRI$  is the azimuth slow time variable.

$$S_T(\tau) = \text{rect}\left(\frac{\tau}{T_p}\right) \exp\left(j2\pi f_c \tau + j\pi K_s \tau^2\right) \quad (1)$$

The received signal of the  $i$ th azimuth sub-beam can be written as Equation (2), in which  $\sigma$  represents the target’s backscattering coefficient,  $c$  is the speed of light,  $\lambda$  is the wavelength,  $R(\eta)$  is the instantaneous slant range from the target to the phase center of the antenna,  $\theta$  is the instantaneous azimuth angle of the target,  $\theta_i$  is the squint angle of the  $i$ th ( $i = 1, \dots, N_a$  and  $N_a$  is the sub-beam number) receiving sub-beam ( $\theta_i > 0$  for forward

looking and  $\theta_i < 0$  for backward looking),  $A_t(\theta)$  represents the transmitting antenna mode, and  $A_{r,i}(\cdot)$  represents  $i$ th the receiving sub-beam's antenna mode.

$$S_i(\tau, \eta) = \sigma \text{rect}\left(\frac{\tau - 2R(\eta)/c}{T_p}\right) A_t(\theta) A_{r,i}(\theta - \theta_i) \cdot \exp\left\{j\pi K_s\left(\tau - \frac{2R(\eta)}{c}\right)^2\right\} \exp\left\{-j\frac{4\pi R(\eta)}{\lambda}\right\} \quad (2)$$

According to the antenna theory, the ideal antenna amplitude mode in the azimuth direction can be represented as Equation (3), in which  $\sin c(\cdot) \triangleq \frac{\sin(\pi x)}{\pi x}$ ,  $D_t$  and  $D_r$  are the lengths of the transmitting and receiving antenna, respectively. In this paper, we mainly discuss the azimuth processing method in the SPC MAB mode; for the sake of simplicity, only the azimuth transmitting and receiving patterns are considered here.

$$\begin{cases} A_t(\theta) = \sin c\left(\frac{D_t \sin \theta}{\lambda}\right) \\ A_{r,i}(\theta) = \sin c\left(\frac{D_r \sin(\theta - \theta_i)}{\lambda}\right) \end{cases} \quad (3)$$

The relationship between  $\theta$  and  $\eta$  can be represented as Equation (4), in which  $V_s$  is the speed of the satellite,  $\eta_c$  is the target's beam center cross time, and  $R_c$  is the shortest slant range between the target and the antenna.

$$\sin \theta = -\frac{V_s \cdot (\eta - \eta_c)}{R(\eta - \eta_c)} = -\frac{V_s(\eta - \eta_c)}{\sqrt{V_s^2(\eta - \eta_c)^2 + R_c^2}} \quad (4)$$

According to the SAR imaging geometry shown in Figure 1, the target's instantaneous Doppler frequency,  $f_a$ , can be calculated as Equation (5). When  $V_s$  and  $\lambda$  are determined,  $f_a$  is only relevant with the angle  $\theta$  between the target and the total azimuth beam center.

$$\sin \theta = \frac{\lambda f_a}{2V_s} \Leftrightarrow f_a = \frac{2V_s \sin \theta}{\lambda} \quad (5)$$

Transferring Equation (2) to the range Doppler (RD) domain through range FFT, azimuth FFT and range IFFT operations in sequence, the sub-beam signal in the RD domain can be obtained as Equation (6):

$$S_i(\tau, f_a) = A \text{rect}\left\{\frac{1}{(1-ZK_s)T_p}\left[\tau - \frac{2R(f_a)}{c}\right]\right\} \cdot H_i(f_a) \cdot \exp\left[-j\frac{4\pi R_0 D(f_a)}{\lambda}\right] \cdot \exp\left[j\pi K_m\left(\tau - \frac{2R(f_a)}{c}\right)^2\right] \exp(-j2\pi f_a \eta_c) \quad (6)$$

In Equation (6),  $f_a$  is the Doppler frequency,  $H_i(f_a)$  is the transmission function of the  $i$ th sub-beam,  $D(f_a)$  is the target's range migration factor,  $Z(f_a)$  is the second range compression factor,  $K_s$  is the transmitted chirp modulation rate, and  $K_m$  is the new chirp modulation rate in the RD domain. Their detailed expressions are as follows:

$$f_a \in \frac{2V_s}{\lambda} [\sin \theta_{start}, \sin \theta_{end}]$$

$$D(f_a) = \sqrt{1 - \left(\frac{\lambda f_a}{2V_s}\right)^2} \triangleq \cos \theta$$

$$Z(f_a) = R_0 \frac{2\lambda \sin^2 \theta}{c^2 \cos^3 \theta}$$

$$\frac{1}{K_m} = \frac{1}{K_s} - \frac{1}{Z} = \frac{1}{K_s} - \frac{1}{R_0} \frac{c^2 \cos^3 \theta}{2\lambda \sin^2 \theta}$$

The sub-beam signal can be defined as follows:

$$S_i(\tau, f_a) = H_i(f_a) S_R(\tau, f_a) \quad (7)$$

In Equation (7),

$$\begin{aligned} S_R(\tau, f_a) = & \text{Arect} \left\{ \frac{1}{(1-ZK_s)T_p} \left[ \tau - \frac{2R(f_a)}{c} \right] \right\} \\ & \cdot \exp \left[ -j \frac{4\pi R_0 D(f_a)}{\lambda} \right] \cdot \exp \left[ j\pi K_m \left( \tau - \frac{2R(f_a)}{c} \right)^2 \right] \\ & \cdot \exp(-j2\pi f_a \eta_c) \end{aligned} \quad (8)$$

$S_R(\tau, f_a)$  is the target's echo during the whole synthetic aperture that is determined by the transmitting beam. The sub-beam echo,  $S_i(\tau, f_a)$ , is weighted by its transmission function,  $H_i(f_a)$ . The bandwidth of  $H_i(f_a)$  is determined by the sub-beam's beam width. Its Doppler frequency center is determined by the corresponding beam center angle  $\theta_i$ . The sub-beam's Doppler frequency position is as follows:

$$f_a \in [f_{a,start,i}, f_{a,end,i}] \quad (9)$$

In Equation (9),

$$f_{a,start,i} = \frac{2V_s}{\lambda} \sin \left( \theta_i - \frac{\theta_a}{2} \right)$$

$$f_{a,end,i} = \frac{2V_s}{\lambda} \sin \left( \theta_i + \frac{\theta_a}{2} \right)$$

The sub-beam's Doppler center frequency,  $f_{a,c,i}$ , and bandwidth,  $f_{a,bw,i}$ , can be calculated as follows:

$$f_{a,c,i} = \frac{V_s}{\lambda} \left[ \sin \left( \theta_i + \frac{\theta_a}{2} \right) + \sin \left( \theta_i - \frac{\theta_a}{2} \right) \right] \quad (10)$$

$$f_{a,bw,i} = \frac{2V_s}{\lambda} \left[ \sin \left( \theta_i + \frac{\theta_a}{2} \right) - \sin \left( \theta_i - \frac{\theta_a}{2} \right) \right] \quad (11)$$

According to the previous analysis, it is found that each sub-beam is equivalent to a band-pass filter whose transmission function is  $H_i(f_a)$ . The sub-beam Doppler bandwidth is  $1/N_a$  of that of the total transmitting beam. Thus, each sub-beam's echo can be sampled by a lower PRF as shown in Equation (12):

$$PRF = k_a \frac{2V_s}{N_a D_t} = k_a \frac{V_s}{N_a \rho_a} \leftrightarrow T_1 = \frac{1}{PRF} = \frac{N_a \rho_a}{k_a V_s} \quad (12)$$

The under-sampled azimuth sub-beam signals are expressed as  $S_{i,ds}(\tau, \eta_1)$ , as shown in Figure 2, in which  $\eta_1$  is the under-sampled slow time variable. The lower PRF or the wider pulse repeat interval  $T_1$  can be used for wide-swath imaging. When all sub-beam Doppler bands are combined, the azimuth high resolution,  $\rho_a$ , can be obtained simultaneously. This is the reason why SPC MAB is a wildly accepted candidate for HRWS imaging. The signal mode in the SPC MAB system is shown in Figure 2.

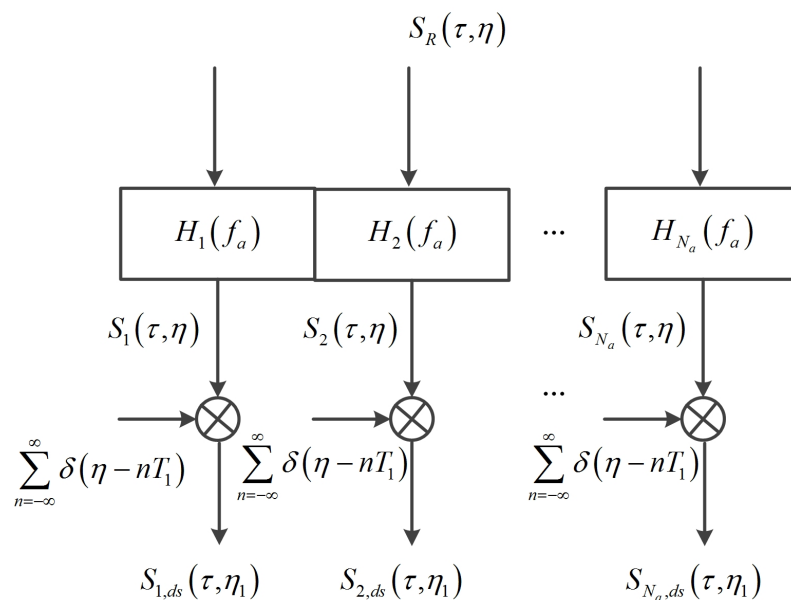


**Figure 2.** Signal mode of SPC MAB.

### 3. Azimuth DBF Filters Design for SPC MAB Mode

In order to obtain an azimuth high-resolution image, the azimuth sub-beam signals,  $S_{i,ds}(\tau, \eta_1)$ , should be assembled to obtain an  $N_a$  times wider Doppler band. The traditional methods, i.e., the combination and the STAP schemes, are described first in this section. Their disadvantages are discussed in detail. After that, the proposed method based on the low-pass band, limited signal spectrum reconstruction theory is delivered.

#### 3.1. Traditional Combination Scheme

Because all the sub-beam echoes are actually sampled with a PRF that satisfies the Nyquist sampling theory, the direct method is to combine all the sub-beam signals. The processing steps of the combination scheme are shown in Figure 3.

First, the under-sampled signals' Doppler bands are shifted to the zero-centered position. The shift step is carried out in the two-dimensional time domain with the compensation functions as follows:

$$H_{DC,i}(\tau, \eta_1) = \exp(-j2\pi f_{a,c,i}\eta_1) \quad (13)$$

Then, the sub-beam signals are up-sampled with a factor  $N_a$ . The up-sampling step is implemented in the azimuth time domain by inserting  $N_a - 1$  zeros between every two original samples. After the up-sampling step, a low-pass filtering step should be followed. Here, the FIR low-pass filters are designed to filter the mirrored spectrum generated by the interpolation steps. Then, all the sub-beam signals are shifted back to their original positions with the compensation functions as follows:

$$H_{BS,i}(\tau, \eta) = \exp(j2\pi f_{a,c,i}\eta) \quad (14)$$

where  $\eta$  represents the up-sampled slow time variable. After transferring to the range Doppler domain with azimuth FFT operations,  $S_{N_a,ds}(\tau, f_\eta)$  are obtained through a summing operation. After the azimuth inverse FFT operation, the azimuth reconstructed signal is as  $\hat{S}_R(\tau, \eta)$ .

From the previous analysis, we can find that the combination scheme regards that all sub-beam azimuth signals are band-limited. In fact, they are not due to the existence of the side-lobes. The spectrum in the main-lobes would be overlapped by those of the side-lobes, although the FIR low-pass filters are adopted. The folded signals are called

azimuth ambiguities. When the sub-beam signals are combined directly, the azimuth ambiguities would result in the fake targets in the final focused image.

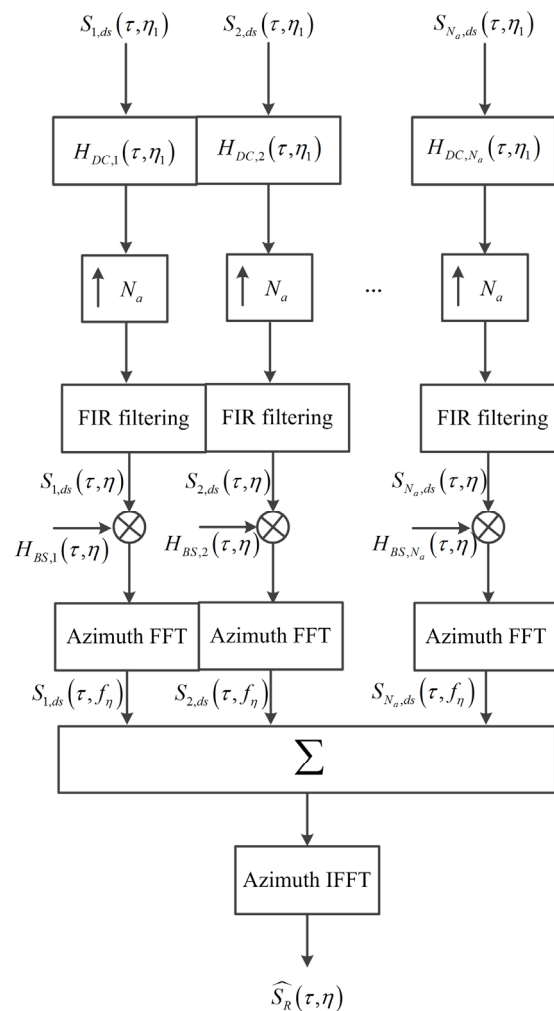


**Figure 3.** The flowchart of the combination scheme.

### 3.2. Traditional STAP Scheme

The traditional STAP method can also be employed to reconstruct the total azimuth spectrum for the SPC MAB mode with a reflector antenna because the sub-beams or the feeds of the reflector antenna can be regarded as the sub-arrays in the linear phase array antenna, although they illuminate different parts of the reflector [30].

The classic beam-formers are known as a minimum variance distortionless response (MVDR) beam-former, based on Capon's method. This method preserves the interest signal and maximizes the SNR. The optimum conjugate complex weight vector,  $w$ , is given as follows:

$$w^* = \frac{\mathbf{R}_v^{-1}(f_a)\mathbf{a}(\theta)}{\mathbf{a}^H(\theta)\mathbf{R}_v^{-1}\mathbf{a}(\theta)} \quad (15)$$

where  $\mathbf{R}_v(f_a)$  is the noise covariance matrix, which is typically unknown and should be replaced by the channel covariance matrix  $\mathbf{R}_u(f_a)$ .  $\mathbf{a}(\theta)$  is the antenna steering vector. In the SPC MAB system with the reflector antenna,  $\mathbf{a}(\theta)$  is mainly determined by the amplitude

of the sub-beams, which is much different from that of the linear phase array.  $\mathbf{R}_u(f_a)$  can be estimated by the sample covariance matrix from the range bins:

$$\hat{\mathbf{R}}_u(f_a) = \frac{1}{K} \sum_{k=1}^K s(f_a, k) s^H(f_a, k)$$

where  $K$  represents the number of the range bins used for the estimation. It should satisfy  $K \geq 2N_a - 1$  [31].  $\mathbf{a}(\theta)$  can be related to the Doppler frequency through the following:

$$f_a = \frac{2V_s \sin \theta}{\lambda}$$

Because the MVDR method only considers the interest direction, the ambiguities are not suppressed or may even be amplified in the worst case. The MVDR method is not the best choice for the SPC MAB azimuth spectrum reconstruction.

Another classic beam-former is the linear constraint minimum variance (LCMV) beam-former [31]. It considers both the extracting of the interest signal and the suppressing of the ambiguities. The optimum conjugate complex weight vector,  $w$ , is as follows:

$$w^* = \mathbf{R}_u^{-1}(f_a) \mathbf{A}(\theta) \left( \mathbf{A}^H(\theta) \mathbf{R}_u^{-1}(f_a) \mathbf{A}(\theta) \right)^{-1} \mathbf{C} \quad (16)$$

In Equation (16),  $\mathbf{C} = [1 \ 0 \ \cdots \ 0]^T$  and  $\mathbf{A}(\theta)$  is

$$\mathbf{A}(\theta) = [\mathbf{a}(\theta) \ \mathbf{a}(\theta_{ab,1}) \ \cdots \ \mathbf{a}(\theta_{ab,N_a-1})] \quad (17)$$

where  $\theta_{ab,1} \sim \theta_{ab,N_a-1}$  represents the directions of the ambiguities. The key step of this method is the calculation of the inverse matrix of  $\mathbf{A}^H(\theta) \mathbf{R}_u^{-1}(f_a) \mathbf{A}(\theta)$ . Even the channels are well balanced, and the number of directions to be suppressed is lower than the number of channels; this matrix can become ill-posed quickly because of the strong focusing effect of the reflector antenna. A possible solution may be the eigenvalue thresholding technologies [32], which increase the computation complexities. Furthermore, in this method, for different Doppler frequency bins, two matrix inverse calculations are involved, i.e.,  $\mathbf{R}_u^{-1}(f_a)$  and  $\left( \mathbf{A}^H(\theta) \mathbf{R}_u^{-1}(f_a) \mathbf{A}(\theta) \right)^{-1}$ ; the calculation efficiencies are much lower than the proposed method.

### 3.3. Low-Pass, Band-Limited Signal Spectrum Reconstruction Model

In the literature [15], Krieger took advantage of the low-pass, band-limited signal spectrum reconstruction theory [29] and analyzed the azimuth spectrum reconstruction method for DPC MAB mode. In this paper, we extend this theory to the SPC MAB mode to design the azimuth DBF filters for each sub-beam. The proposed method and the DPC MAB solution, i.e., named as the multiple-channel reconstruction algorithm (MCRA) in the literature [15], are both based on the low-pass, band-limited signal spectrum reconstruction theory. The differences between them lie in the following. (1) The input signals of the MCRA are all under-sampled, while in the SPC MAB mode, the signal input is all well-sampled. (2) The transfer functions of the MCRA are based on the transmission delays that are determined by the distances between the receiving antennas and the transmitting antenna. In SPC MAB, all the channels share the same phase center; the differences between all channels are determined by the two-way antenna modes. Thus, in the SPC MAB, the reconstruction filters for all channels are quite different from those of the DPC MAB mode. (3) The goals are different. The goal of the MCRA is to reconstruct the whole Doppler bandwidth from the aliased sub-beam signals, while the goal of the proposed method is to combine all the well-sampled, sub-beam signals well and depress the inter-interference between all the sub-beams simultaneously.

### 3.3.1. Analysis of Transfer Functions

In the SPC MAB, the input signal  $S_R(\tau, f_a)$  is as Equation (8). Before the under-sampling step, we can obtain  $N_a$  versions of  $S_R(\tau, f_a)$  by weighting it with all sub-beam transmission functions  $H_i(f_a)$  ( $i = 1, \dots, N_a$ ). Then, the  $N_a$  versions of  $S_R(\tau, f_a)$  are obtained with a PRF of approximately  $1/N_a$  of the total azimuth bandwidth  $B_{d,total}$  that is determined by the transmitting beam width as shown in Figure 2. The signal model is consistent with the low-pass, band-limited signal spectrum reconstruction theory. And the transmission functions can meet the requirements described in the literature [29]. Thus, once the reconstruction filters  $P_i(f_a)$  ( $i = 1, \dots, N_a$ ) are designed correctly, we can reconstruct the original azimuth wide band signal, and the inter-beam interference and ambiguities can be suppressed simultaneously.

Because the design of reconstruction filters is relevant to the sub-beam transmission functions  $H_i(f_a)$ , they are analyzed in detail first. From the previous analysis, the weight coefficients of all sub-beams to the input signal are finished in the azimuth time domain as Equation (18).

$$\begin{aligned} S_i(\tau, \eta) &= A_t(\theta) A_i(\theta - \theta_i) S_T(\tau, \eta) \\ &= \sin c\left(\frac{D_t \sin \theta}{\lambda}\right) \sin c\left(\frac{D_r \sin(\theta - \theta_i)}{\lambda}\right) S_T(\tau, \eta) \\ &\triangleq A_{tr,i}(\theta) S_T(\tau, \eta) \end{aligned} \quad (18)$$

Due to the fact that  $A_{tr,i}(\theta)$  only affects the amplitude of the input signal, the phase of the signal and the stationary phase point are not affected. The transmission functions in the Doppler frequency domain can be obtained through replacing  $\theta$  by  $f_a$  with  $\sin \theta = \frac{\lambda f_a}{2V_s}$  as Equation (19), which holds only under the narrow-band assumption.

$$H_i(f_a) = \sin c\left(\frac{D_t \sin \theta}{\lambda}\right) \sin c\left(\frac{D_r \sin(\theta - \theta_i)}{\lambda}\right) \Big|_{\sin \theta = \frac{\lambda f_a}{2V_s}} \quad (19)$$

Once the transferring functions are determined, the reconstruct filters  $P_i(f_a)$  can be designed for all the azimuth channels.

### 3.3.2. Design of the DBF Filters

According to the low-pass, band-limited signal spectrum reconstruction theory, the DBF filters can be obtained from the inverse matrix of the transferring function matrix as shown in Equation (20):

$$\mathbf{H}(f_a) = \begin{bmatrix} H_1(f_a) & \cdots & H_{N_a}(f_a) \\ \vdots & \cdots & \vdots \\ H_1(f_a + (N_a - 1)PRF) & \cdots & H_{N_a}(f_a + (N_a - 1)PRF) \end{bmatrix} \quad (20)$$

The inverse matrix of Equation (20) is as Equation (21):

$$\mathbf{H}^{-1}(f_a) = \begin{bmatrix} A_{11}(f_a) & \cdots & A_{1N_a}(f_a) \\ \cdots & \cdots & \cdots \\ A_{N_a1}(f_a) & \cdots & A_{NN_a}(f_a) \end{bmatrix} \quad (21)$$

Set the reconstruction filters as Equation (22):

$$\mathbf{P}(f_a) = \begin{bmatrix} P_1(f_a) \\ \cdots \\ P_{N_a}(f_a) \end{bmatrix} \quad (22)$$

In Equation (22),  $P_j(f_a)$  represents the  $j$ th sub-beam reconstruction filter. Each filter can be divided into  $N_a$  parts. The  $k$ th ( $k = 1, \dots, N_a$ ) part of  $P_j(f_a)$  can be obtained by the  $j$ th row and  $k$ th column component in  $H^{-1}(f_a)$ , i.e.,  $A_{jk}(f_a)$  as follows:

$$P_j(f_a + (k-1)f_s) = A_{jk}(f_a), f_a \in I_1 \quad (23)$$

In Equation (23),  $I_1$  is as follows:

$$I_1 = [-N_a \cdot PRF/2, -(N_a - 2) \cdot PRF/2] \quad (24)$$

Substituting  $f_a + (k-1)f_s$  with  $f'_a$  in Equation (23), we can obtain a more comprehensive equation of Equation (23) as Equation (25):

$$P_j(f'_a) = A_{jk}(f'_a - (k-1)PRF), f'_a \in I_k \quad (25)$$

In Equation (25),

$$I_k = \left[ -\frac{N_a \cdot PRF}{2} + (k-1)PRF, -\frac{N_a \cdot PRF}{2} + k \cdot PRF \right] \quad (26)$$

Thus, the complete filter for the  $j$ th sub-beam can be represented as follows:

$$P_j(f_a) = \sum_k A_{jk}(f_a - (k-1)PRF), f_a \in I_k \quad (27)$$

Now we take  $N_a = 2$  as an example to show the filters' design for the sub-beams. The transferring functions can be written as follows:

$$\begin{cases} H_1(f_a) = \sin c \left[ \frac{D_a}{2V_s} \left( f_a + \frac{B_d}{4} \right) \right]^2 \\ H_2(f_a) = \sin c \left[ \frac{D_a}{2V_s} \left( f_a - \frac{B_d}{4} \right) \right]^2 \end{cases} \quad (28)$$

The corresponding transferring function matrix is as Equation (29):

$$\mathbf{H}(f_a) = \begin{bmatrix} \sin c \left[ \frac{D_a}{2V_s} \left( f_a + \frac{B_d}{4} \right) \right]^2 & \sin c \left[ \frac{D_a}{2V_s} \left( f_a - \frac{B_d}{4} \right) \right]^2 \\ \sin c \left[ \frac{D_a}{2V_s} \left( f_a + \frac{B_d}{4} + PRF \right) \right]^2 & \sin c \left[ \frac{D_a}{2V_s} \left( f_a - \frac{B_d}{4} + PRF \right) \right]^2 \end{bmatrix} \quad (29)$$

According to the conclusion in Equation (25), the filters for sub-beam 1 and 2 can be calculated as Equation (30) and Equation (31), respectively.

$$P_1(f_a) = \begin{cases} \frac{\sin c \left[ \frac{D_a}{2V_s} \left( f_a - \frac{B_d}{4} + PRF \right) \right]^2}{\sin c \left[ \frac{D_a}{2V_s} \left( f_a + \frac{B_d}{4} \right) \right]^2 \sin c \left[ \frac{D_a}{2V_s} \left( f_a - \frac{B_d}{4} + PRF \right) \right]^2 - \sin c \left[ \frac{D_a}{2V_s} \left( f_a - \frac{B_d}{4} \right) \right]^2 \sin c \left[ \frac{D_a}{2V_s} \left( f_a + \frac{B_d}{4} + PRF \right) \right]^2}, -PRF < f_a < 0 \\ \frac{-\sin c \left[ \frac{D_a}{2V_s} \left( f_a - \frac{B_d}{4} - PRF \right) \right]^2}{\sin c \left[ \frac{D_a}{2V_s} \left( f_a + \frac{B_d}{4} - PRF \right) \right]^2 \sin c \left[ \frac{D_a}{2V_s} \left( f_a - \frac{B_d}{4} - PRF \right) \right]^2 - \sin c \left[ \frac{D_a}{2V_s} \left( f_a - \frac{B_d}{4} \right) \right]^2 \sin c \left[ \frac{D_a}{2V_s} \left( f_a + \frac{B_d}{4} \right) \right]^2}, 0 < f_a < PRF \end{cases} \quad (30)$$

$$P_2(f_a) = \begin{cases} \frac{-\sin c \left[ \frac{D_a}{2V_s} \left( f_a + \frac{B_d}{4} + PRF \right) \right]^2}{\sin c \left[ \frac{D_a}{2V_s} \left( f_a + \frac{B_d}{4} \right) \right]^2 \sin c \left[ \frac{D_a}{2V_s} \left( f_a - \frac{B_d}{4} + PRF \right) \right]^2 - \sin c \left[ \frac{D_a}{2V_s} \left( f_a - \frac{B_d}{4} \right) \right]^2 \sin c \left[ \frac{D_a}{2V_s} \left( f_a + \frac{B_d}{4} + PRF \right) \right]^2}, -PRF < f_a < 0 \\ \frac{\sin c \left[ \frac{D_a}{2V_s} \left( f_a + \frac{B_d}{4} - PRF \right) \right]^2}{\sin c \left[ \frac{D_a}{2V_s} \left( f_a + \frac{B_d}{4} \right) \right]^2 \sin c \left[ \frac{D_a}{2V_s} \left( f_a - \frac{B_d}{4} - PRF \right) \right]^2 - \sin c \left[ \frac{D_a}{2V_s} \left( f_a - \frac{B_d}{4} \right) \right]^2 \sin c \left[ \frac{D_a}{2V_s} \left( f_a + \frac{B_d}{4} - PRF \right) \right]^2}, 0 < f_a < PRF \end{cases} \quad (31)$$

After filtering by the corresponding filters, the reconstructed azimuth signal can be obtained by summing all the filtered signals.

### 3.3.3. Strategies for Non-Ideal Antenna Patterns Situation

In Section 3.3.2, we analyzed the ideal antenna pattern situation. In fact, the real transmitting and receiving antenna modes are much different from the ideal  $\sin c(\cdot)$  functions, especially for the reflector antennas.

In the reflector-feed antenna system, there exist two major factors leading to this mismatch. One is the surface deviation that is mainly affected by the manufacture accuracy and the installation offset. The other one is the magnitude inconsistency and phase difference between the sub-beams.

Figure 4 shows the ideal antenna patterns compared with the real measurements. The ideal transmitting and receiving patterns are shown in Figure 4a,b. The transmitting beam is much wider than the receiving beams through activating more azimuth feeds. They are all in ideal  $\sin c(\cdot)$  function form. In contrast, as shown in Figure 4c,d, the measurements are quite different. The amplitude of the real transmitting is approximately 5 dB lower than the ideal one because the actual electronic diameter is shorter than the ideal one and the antenna efficiency is much lower than 50%. The transmitting beam amplitude undulates within  $23.575 \pm 0.75$  dB. On the other hand, the receiving sub-beams' amplitudes are not equal to each other, and the cross point of the sub-beams is approximately  $-4$  dB. The squint angles of all sub-beams differ from the ideal ones due to the installation offset, which results in the differences of the Doppler frequency centers.

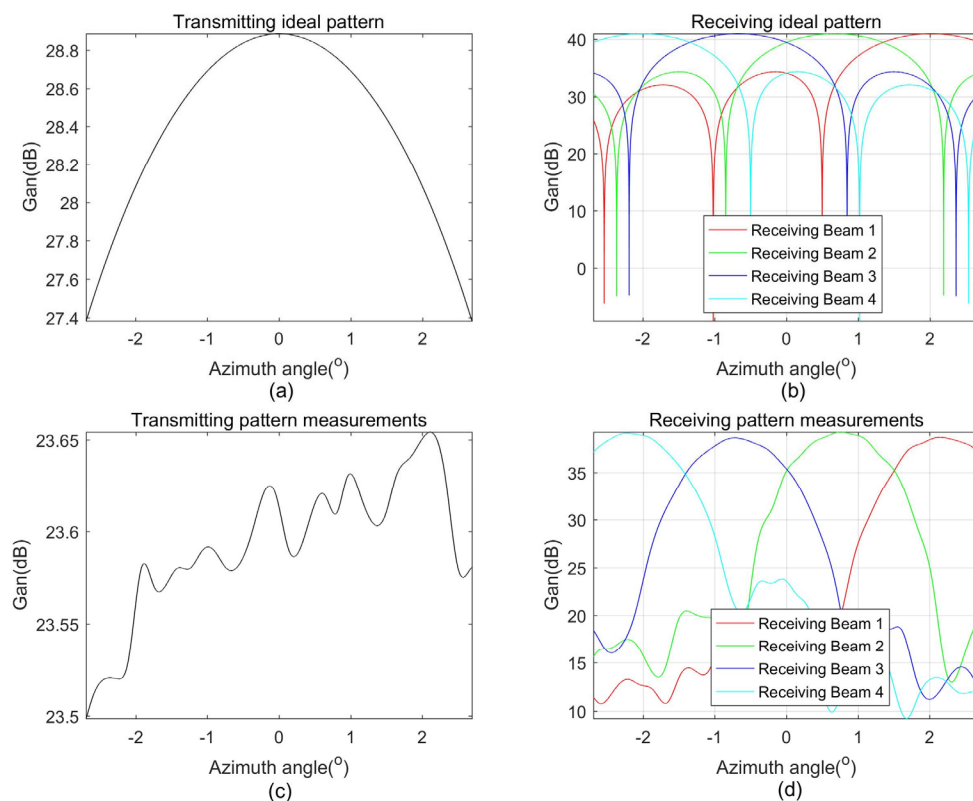


**Figure 4.** Antenna pattern comparison: (a,b) The ideal transmitting/receiving antenna pattern; (c,d) The measured transmitting/receiving antenna patterns.

If the ideal  $H_i(f_a)$  was used to process the echoes obtained with the non-ideal antenna modes directly, the mismatch would result in the huge errors in the ambiguities suppression and the spectrum reconstruction.

Thus, in the real raw data focusing, the real antenna modes should be used. They can be obtained by far field radiation pattern measurement. Normally, they are obtained in the

azimuth angle domain as shown in Equation (32), in which  $A_{mT}(\theta)$ ,  $A_{mR,i}(\theta)$  and  $H_{mi}(\theta)$  are the transmitting and the  $i$ th sub-beam's receiving and two-way pattern, respectively:

$$H_{mi}(\theta) = A_{mT}(\theta)A_{mR,i}(\theta) \quad (32)$$

Normally, again, the sampling frequency of the variable  $\theta$  is not high enough to match the requirement of the real azimuth sampling rate, i.e., PRF. Thus, the measured radiation patterns should be up-sampled through the interpolation method first.

After the interpolations, according to the relationship of the azimuth angle  $\theta$  and the Doppler frequency  $\sin \theta = \frac{\lambda f_a}{2V_s}$ , we can obtain the sub-beam transferring functions in the Doppler frequency domain as follows:

$$H_i(f_a) = H_i(\theta) \Big|_{f_a = \frac{2V_s \sin \theta}{\lambda}} \quad (33)$$

However, as described in Section 3.3.2, Equation (33) holds only under the narrow-band assumption. In order to improve the calculation precision of  $H_i(f_a)$ , the sub-beam weighting function  $H_i(\eta)$  in the azimuth time domain is calculated first as Equation (34), in which  $\eta = -\frac{R_0 \tan \theta}{V_s}$  gives the relationship between the azimuth time variable  $\eta$  and the azimuth angle  $\theta$  in the slant range plane:

$$H_i(\eta) = H_i(\theta) \Big|_{\eta = -\frac{R_0 \tan \theta}{V_s}} \quad (34)$$

Then, the corresponding azimuth echoes  $S_{az,i}(\eta)$  of the sub-beams are as Equation (35):

$$S_{az,i}(\eta) = H_i(\eta)S_{az}(\eta) \quad (35)$$

In Equation (35),

$$\begin{aligned} S_{az}(\eta) &= \exp \left\{ -j \frac{4\pi R_i(\eta)}{\lambda} \right\} \\ R_i(\eta) &= \sqrt{V_s^2(\eta - \eta_c)^2 + R_0^2} \end{aligned} \quad (36)$$

Now, we can calculate the results of  $S_{az,i}(\eta)$  and  $S_{az}(\eta)$  in the Doppler frequency domain, respectively, through FFT operations. Then, the accurate results of  $H_i(f_a)$  can be obtained as follows:

$$H_i(f_a) = \frac{\text{fft}(S_{az,i}(\eta))}{\text{fft}(S_{az}(\eta))} \quad (37)$$

The calculated  $H_i(f_a)$ , based on the measured antenna patterns shown in Figure 4, are given in Figure 5.

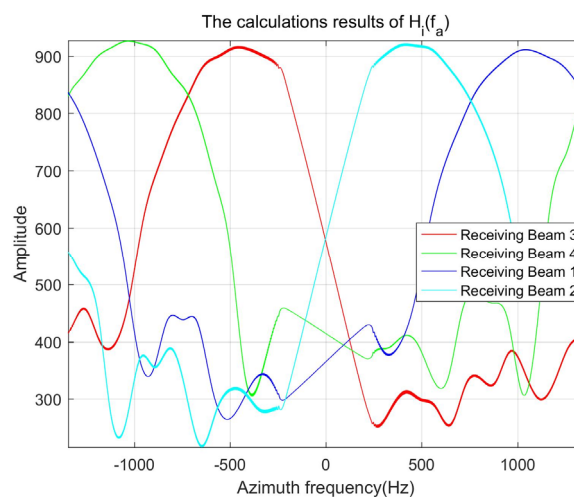


**Figure 5.** The calculated transferring functions of the sub-beams shown in Figure 4c,d.

From the previous analysis, it is found that, no matter if  $H_i(f_a)$  are obtained by Equation (33) or (37), they are not expressed in closed forms but numerical results.  $H_i(f_a)$  and their replicas (shifted by  $(1 \sim (N_a - 1)) \cdot PRF$ ) can be inserted in the DBF matrix shown in Equation (20). After the processing steps described in Equations (21)–(27), the DBF filters for all azimuth sub-beams can be obtained. After filtering by the corresponding filters and summing all the filtered signals, the reconstruction and inter-interference depressing procedure finishes.

In short, when the antenna's radiation patterns are non-ideal, they can be obtained by far field radiation pattern measurement. The corresponding transferring functions are numerical results. As long as the real ones are measured correctly, the proposed method described in Section 3.3.2 is still valid. The reconstruction procedure is shown in Figure 6.

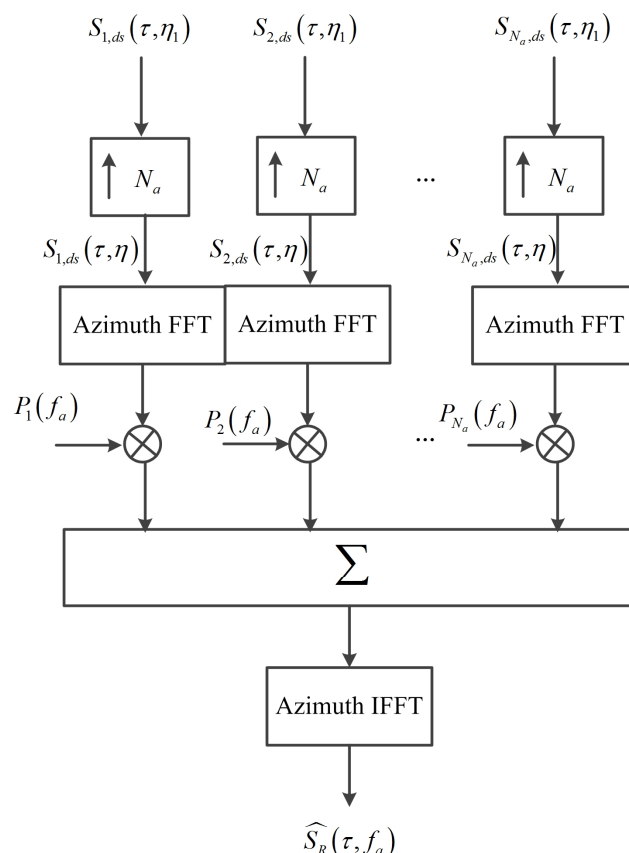


**Figure 6.** The flowchart of the proposed reconstruction method.

#### 4. Simulations and Results

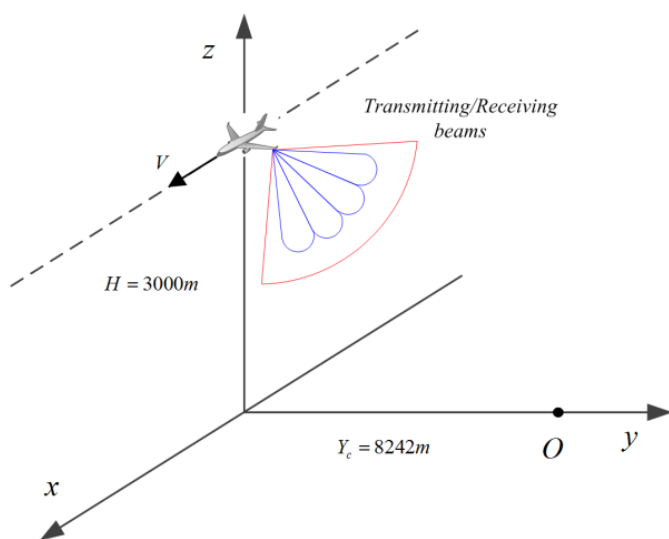
In order to verify the validities of the proposed method, both for ideal and non-ideal antenna modes, simulations are carried out in this section.

The simulations are based on an airborne SAR system with a reflector antenna with  $4 \times 4$  (elevation  $\times$  azimuth) feeds that were designed and manufactured in 2021. The carrier frequency is in the  $K_a$  band. The antenna diameter is approximately 0.4 m. The other parameters of the airborne system are shown in Table 1.

The imaging geometry for the simulations is shown in Figure 7. The scene center is set at point O. The PRF is selected as 670 Hz, which is 1.2 times the sub-beam's Doppler bandwidth. This system can obtain 1.3 m ground resolution and approximately 0.08 azimuth resolution.

**Table 1.** Ground test SAR system.

Parameter	Value	Unit
Platform height	3	Km
Platform velocity	100	m/s
Reflector diameter	0.316	m
Carry frequency	35.0	GHz
Azimuth channel	4	-
Elevation channel	4	-
Center looking angle	70	°
Azimuth resolution	0.316/4	m
Swath width	2.4	Km
Pulse duration	1	us
Signal bandwidth	120	MHz
PRF	670	Hz

**Figure 7.** The imaging geometry for simulations.

#### 4.1. Point Target Simulation

##### 4.1.1. Simulations for Ideal Antenna Mode

The echoes received by the sub-beams of the point target locating at O are generated first. The transmitting and receiving antenna modes are shown in Figure 4a,b, which are all in ideal  $\text{sinc}(\cdot)$  forms. The simulations are implemented along the azimuth direction. Figure 8 gives the results. In Figure 8a, the reconstructed Doppler band by the combination scheme is provided, comparing it with that of the standard chirp-like azimuth signal. It is found that the combination scheme can obtain a Doppler band like that of the standard chirp signal. However, this method does not consider the inter-interferences between the sub-beams; the reconstructed Doppler band fluctuates inside the bandwidth, which will result in the ambiguities along the azimuth direction. Figure 8c provides the azimuth compression result of the signal obtained as in Figure 8a. Due to the lack of considering the inter-interference, the compression result has two ambiguities beside the main peak, along the azimuth direction, whose amplitudes are approximately  $-12$  dB lower than the main peak. Obviously, these “Ghost” targets will seriously affect the quality of the final focus images. Figure 8b,d give the Doppler band obtained by the proposed method described in Section 3.3.2 and the corresponding azimuth compression result. We can find the proposed method can almost perfectly reconstruct the Doppler band for the SPC MAB mode, except for some little differences at the edge of the Doppler frequency domain. Thus, the azimuth ambiguities disappear in the corresponding azimuth compression result as shown in Figure 8d. In other words, the validities of the proposed method for dealing

with the ideal-antenna mode situation can be verified through the simulations provided in Figure 8.

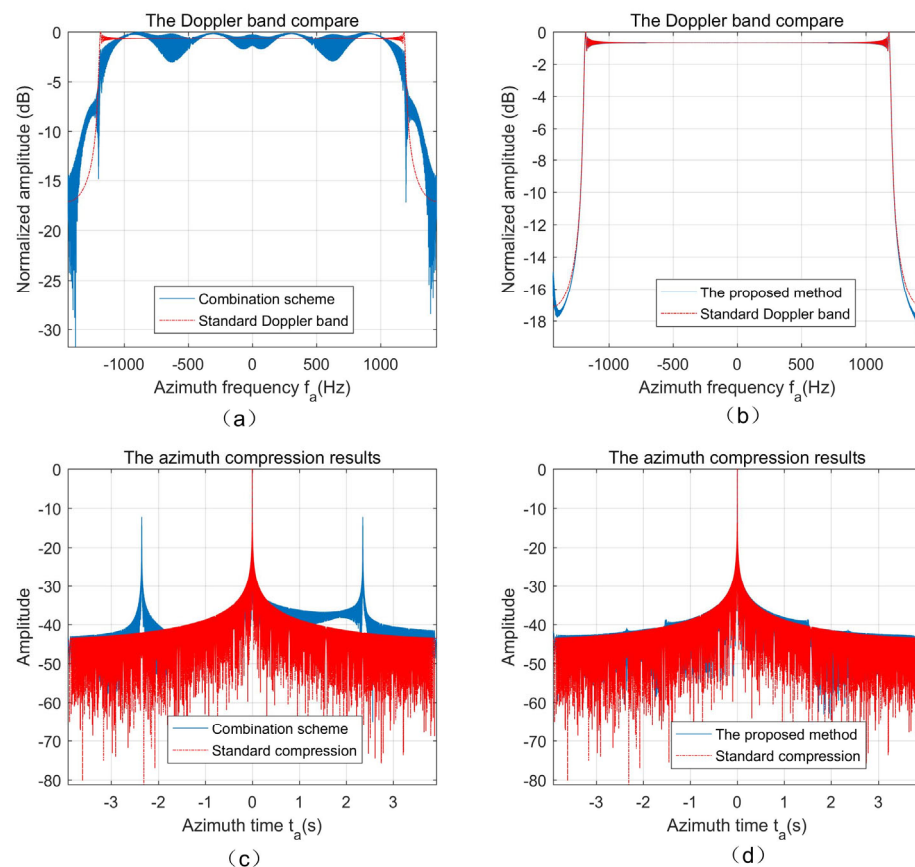


**Figure 8.** The simulations for the ideal antenna mode. (a) The result of the reconstructed Doppler band by the combination scheme; (b) The result of the reconstructed Doppler band by the proposed method described in Section 3.3.2; (c) The azimuth compression result of the combination scheme; (d) The azimuth compression result of the proposed method described in Section 3.3.2.

#### 4.1.2. Simulations for Non-Ideal Antenna Mode

The simulations for the non-ideal antenna mode are based on a prototype reflector antenna with  $4 \times 4$  (elevation  $\times$  azimuth) feeds. The antenna's pattern was measured as shown in Figure 4c,d.

The simulation results processed by the combination scheme and the proposed method are shown in Figure 9. The contour images of the point target up-sampled by eight are shown in (a) and (e), from which we can find that, after pre-processing by both methods, the echoes can be focused correctly. That means that both methods can reconstruct the spectrum well in the principal value interval at least. If the input signal satisfies the band-limited condition strictly, both methods are good candidates for the spectrum reconstruction. The range and azimuth slices of the point target simulations are shown in (b), (c) and (f), (g). It is found both in range and azimuth direction; the focused results are all in  $\text{sinc}(\cdot)$  function form. Finally, shown in (d) and (h), the whole azimuth timeline is extracted from the two-dimensional images. It is found that the combination scheme does not suppress the azimuth ambiguities. Around the focused peak, there are six ambiguities. They are divided into two groups, three on the left and the others on the right side. In this paper, there are four azimuth sub-beams. If not being depressed, the other three sub-beam signals would be aliased with the correct signal. Three azimuth "ghost" targets would appear on each side of the peak. The amplitudes of them are approximately  $-13.92$  dB,  $-19.6$  dB and  $-22.23$  dB, respectively. Generally, the ambiguities should be depressed down to approxi-

mately  $-20$  dB for conventional imaging or at least  $-30$  dB for sea surface target detection. The disadvantages of the combination scheme are obvious. In contrast, the proposed method depresses the azimuth ambiguities down to approximately  $-35.06$  dB. No “ghost” targets exist along the azimuth direction.

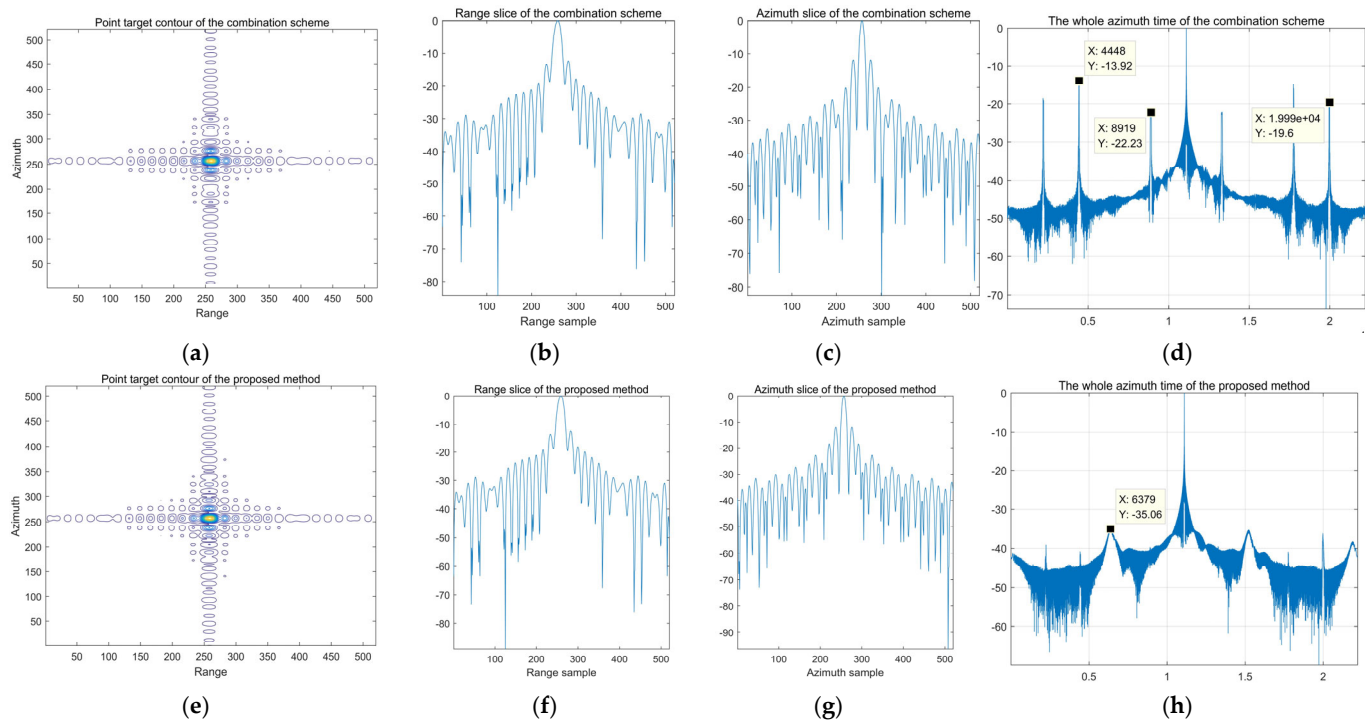


**Figure 9.** The simulation results of the point target at the scene center. (a–d) are the results of the combination scheme; (a) The contour of the point target; (b,c) are the corresponding range and azimuth slices; (d) The whole azimuth time; (e–h) are the results of the proposed method; (e) The contour of the point target; (f,g) are the corresponding range and azimuth slices; (d,h) are the whole azimuth time in the two-dimensional images.

#### 4.2. Distributed Targets Simulation

In order to verify the conclusion in the previous section further, simulations based on the distributed targets are provided in this section with non-ideal antenna patterns. The backscatter coefficients of the targets are extracted from an image obtained by the GF-3 satellite in Zhejiang Province, China, in 2016. The extracted area is a wharf that is approximately  $200 \times 200$  pixels in the original image, as shown in Figure 10.

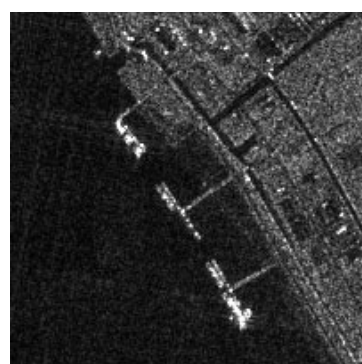


**Figure 10.** The backscatter coefficient of targets extracted from GF-3 satellite images.

The result of the combination scheme is shown in Figure 11. The final image is shown on the left, from which we can find that, except for the normal images in the middle, there are two ambiguous areas. The middle area and the ambiguous areas are zoomed in on the right side of Figure 11. When the azimuth scene becomes larger, the ambiguous areas would be aliased with the original targets, or the other areas' ambiguities would be aliased with the scene center targets. Thus, if the combination scheme is employed to process the raw data, the final image would have serious ambiguous phenomena.

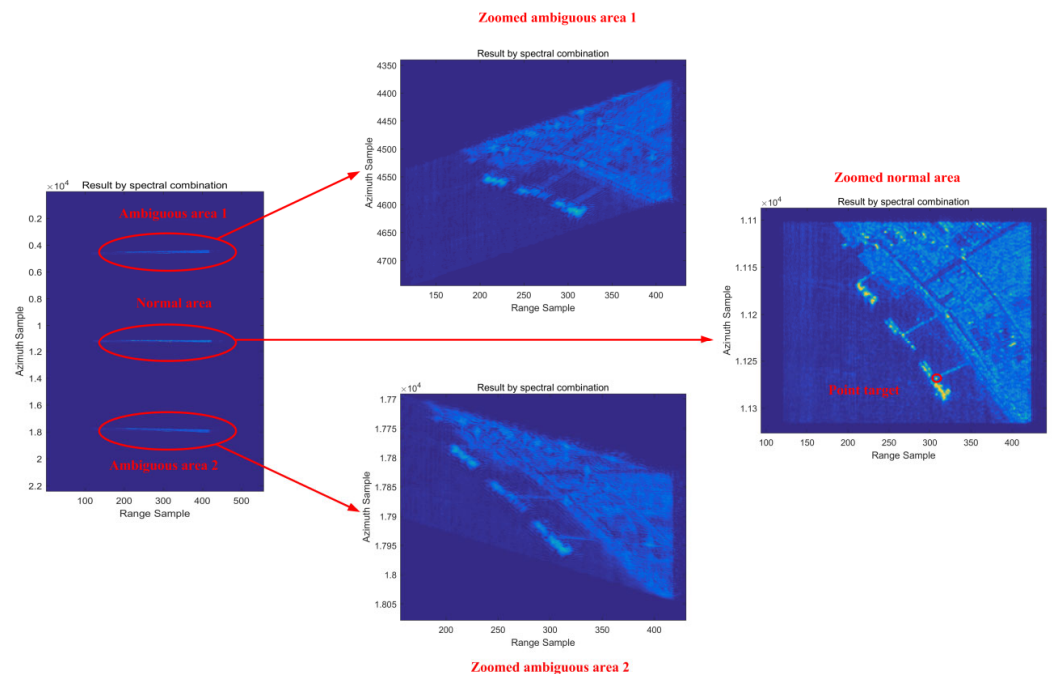


**Figure 11.** The result of the combination scheme.

The result of the proposed method is shown in Figure 12. The final image is shown on the left, from which we can find that, except for the normal images in the middle, no ambiguous area exists. The focused area is zoomed in on the right side of Figure 12. The proposed method considers the spectrum reconstruction and ambiguities suppressing simultaneously.

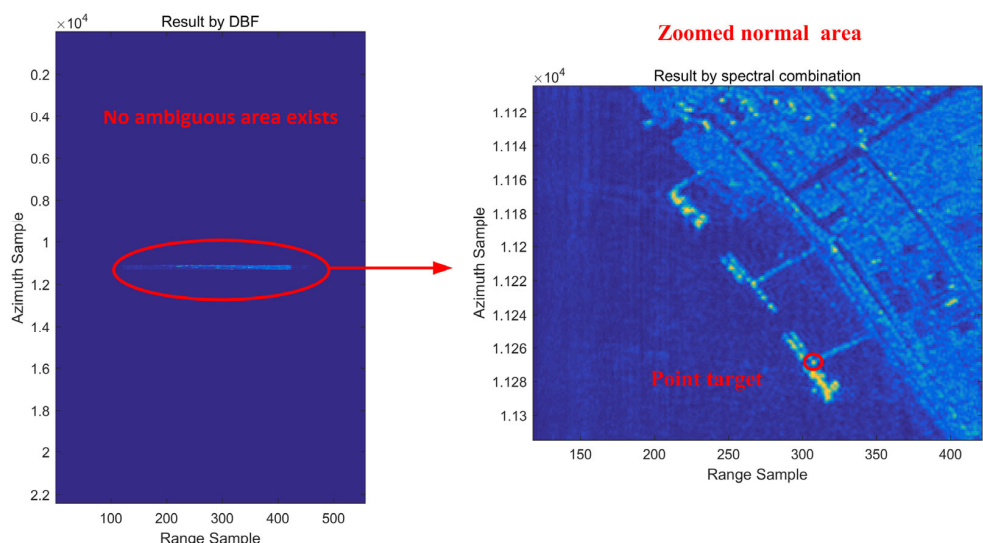


**Figure 12.** The result of the proposed method.

## 5. Conclusions

SPC MAB mode is an effective method for HRWS SAR imaging. In this mode, a wide azimuth beam transmits the radar signal, and multiple azimuth narrow beams receive the echoes. The required PRF needs to be just larger than the Doppler bandwidth of the narrow beams. The decreased PRF can fulfill the wide-swath imaging. The azimuth high resolution can be obtained by combining all the azimuth sub-beam Doppler bandwidths. The conventional azimuth spectrum reconstruction method for the SPC MAB mode with a reflector antenna includes the combination scheme and the STAP method. The combination scheme does not consider the azimuth ambiguities problem, which results in “Ghost” targets along the azimuth direction. The STAP method, i.e., the LCMV beam-former, considers both the extracting of the interest signal and the suppressing of the ambiguities to build the optimum complex weight vector. However, the estimation of the channel covariance matrix  $R_u(f_a)$  and the calculation of the inverse matrix  $A^H(\theta)R_u^{-1}(f_a)A(\theta)$  decrease the calculation efficiency and the robustness of this method dramatically. In this paper, a novel digital beam-forming method based on the basic theory of the low-pass, band-limited, multiple-channel under-sampling and reconstruction is proposed for the SPC MAB imaging mode. The proposed method deals with the ideal antenna modes first. When ideal antenna modes are adopted, the transmitting and receiving beams are all in deal  $\sin c(\cdot)$  function form. Through multiplying the transmitting and the receiving sub-beams’ antenna modes, the transferring functions of the sub-beams can be obtained. They and their replicas are then utilized to form the transferring function matrix  $H(f_a)$ . Then, the elements in the inverse matrix  $H^{-1}(f_a)$  can be used to build the digital beam-forming filters for all the sub-beams. The designed filters can reconstruct the correct wide-bandwidth azimuth spectrum, and the azimuth ambiguities are depressed simultaneously. The proposed method is then extended to the SPC MAB mode with non-ideal antenna patterns because the real antenna patterns are quite different from the ideal ones, especially for a reflector antenna, due to the manufacture accuracy, the installation offset and the magnitude and phase inconsistency difference between the sub-beams. In order to deal with this situation, the far field antenna modes are measured first. According to the measurements, the sub-beam transferring functions are calculated precisely. The calculated transferring functions and their replicas are then used to form the transferring matrix  $H(f_a)$ . The followed processing steps are the same with that of the ideal-antenna modes. The simulation experiments with point target and distributed targets prove the validities of the proposed method both for azimuth spectral reconstruction and the inter-beam interferences suppressing, no matter that the SPC MAB’s antenna mode is ideal or non-ideal.

**Author Contributions:** Conceptualization, W.Z. and C.L.; methodology, W.Z.; software, W.Z., S.Z. and J.L.; validation, D.L. and W.P.; formal analysis, D.Y. and W.P.; investigation, D.L. and W.P.; resources, C.L. and C.D.; data curation, D.L.; writing—original draft preparation, W.Z.; writing—review and editing, W.Z. and C.L.; visualization, J.L.; supervision, C.D.; project administration, W.Z.; funding acquisition, W.Z. and C.L. All authors have read and agreed to the published version of the manuscript.

**Funding:** This work was partly supported by the National Key R&D Program of China under Grant 2022YFB3902400 and was supported by the National Defense Science and Technology Innovation Zone Project of China under Grant 19-H863-01-ZT-002-063-07.

**Data Availability Statement:** The datasets used for analysis during the current study are available from the corresponding author upon reasonable request.

**Acknowledgments:** The authors thank the anonymous reviewers for their valuable comments and suggestions to improve the paper.

**Conflicts of Interest:** The authors declare no conflicts of interest.

## References

- Currie, A.; Brown, M.A. Wide-swath SAR. *Radar and Signal Processing. IEE Proc. F* **1992**, *139*, 122–135.
- Goodman, N.; Rajakrishna, D.; Stiles, J. Wide swath, high resolution SAR using multiple receive apertures. In Proceedings of the International Geoscience and Remote Sensing Symposium, Hamburg, Germany, 28 June–2 July 1999; pp. 1767–1769.
- Suess, M.; Wiesbeck, P. Side-Looking Synthetic Aperture Radar System. European Patent EP1241487, 8 February 2006.
- Krieger, G.; Gebert, N.; Moreira, A. Multidimensional waveform encoding: A new digital beamforming technique for synthetic aperture radar remote sensing. *IEEE Trans. Geosci. Remote Sens.* **2008**, *46*, 31–46. [[CrossRef](#)]
- Yu, K.; Zhu, S.; Lan, L.; Yang, B. High-Resolution and Wide-Swath SAR Imaging with Space-Time Coding Array. *Remote Sens.* **2023**, *15*, 2465. [[CrossRef](#)]
- Younis, M.; Fischer, C.; Wiesbeck, W. Digital beamforming in SAR systems. *IEEE Trans. Geosci. Remote Sens.* **2003**, *41*, 1735–1739. [[CrossRef](#)]
- Krieger, G.; Gebert, N.; Younis, M.; Bordoni, F.; Patyuchenko, A.; Moreira, A. Advanced concepts for ultra-wide-swath SAR imaging. In Proceedings of the 7th European Conference on Synthetic Aperture Radar, Friedrichshafen, Germany, 2–5 June 2008; pp. 1–4.
- Nicolas, G.; Krieger, G.; Moreira, A. Multichannel Azimuth Processing in ScanSAR and TOPS mode operation. *IEEE Trans. Geosci. Remote Sens.* **2010**, *48*, 2994–3008.
- Michelangelo, V.; Krieger, G.; Moreira, A. Staggered-SAR: A new concept for high-resolution wide-swath imaging. In Proceedings of the IET International Conference on Radar Systems, Glasgow, UK, 22–25 October 2012; pp. 1–6.
- Michelangelo, V.; Krieger, G.; Moreira, A. Staggered SAR: High-Resolution Wide-Swath Imaging by Continuous PRI Variation. *IEEE Trans. Geosci. Remote Sens.* **2014**, *52*, 4462–4479.
- Felipe, Q.A.; Tobias, R.; Gerhard, K. Multichannel Staggered SAR: System Concepts with Reflector and Planar Antennas. *IEEE Trans. Aerosp. Electron. Syst.* **2019**, *55*, 877–902.
- Wang, X.; Ruan, Y.; Zhang, X. Accuracy Improvement of High-Resolution Wide-Swath Spaceborne Synthetic Aperture Radar Imaging with Low Pulse Repetition Frequency. *Remote Sens.* **2023**, *15*, 3811. [[CrossRef](#)]
- Ding, C.; Liang, X.; Wang, J.; Chen, L. An novel airborne MIMO-SAR system built in IECAS. In Proceedings of the 2017 International Geoscience and Remote Sensing Symposium, Fort Worth, TX, USA, 23–28 July 2017; pp. 2423–2426.
- Jin, G.; Wang, Y.; Zhu, D.; Niu, S.; Yan, H. A Reconfigurable MIMO-SAR Transmission Scheme Based on Inter-Pulse and Intra-Pulse Joint Phase Modulation. *IEEE Trans. Signal Process.* **2022**, *70*, 4265–4276. [[CrossRef](#)]
- Krieger, G.; Gebert, N.; Moreira, A. Unambiguous SAR signal reconstruction from nonuniform displaced phase center sampling. *IEEE Trans. Geosci. Remote Sens.* **2004**, *1*, 260–264. [[CrossRef](#)]
- Li, Z.; Wang, H.; Su, T.; Bao, Z. Generation of wide-swath and high-resolution SAR images from multichannel small spaceborne SAR systems. *IEEE Geosci. Remote Sens. Lett.* **2005**, *2*, 82–86. [[CrossRef](#)]
- Gebert, N.; Almeida, F.Q.; Krieger, G. Airborne Demonstration of Multichannel SAR Imaging. *IEEE Geosci. Remote Sens. Lett.* **2011**, *8*, 963–967. [[CrossRef](#)]
- Sadowsky, G.A.; Ghaemi, H.; Hensley, S.C. First Results from an Airborne Ka-band SAR using SweepSAR and Digital Beamforming. In Proceedings of the 9th European Conference on Synthetic Aperture Radar, Nürnberg, Germany, 23–26 April 2012; pp. 23–26.
- Wang, H.; Zheng, S.; Dai, S.; Zhao, Y. A New Airborne Ka-band DBF-SAR system and flight test results. In Proceedings of the 12th European Conference on Synthetic Aperture Radar, Aachen, Germany, 5–7 June 2018; pp. 1–5.
- Zhou, Y.; Wang, W.; Chen, Z.; Wang, P.; Zhang, H.; Qiu, J.; Zhao, Q.; Deng, Y.; Zhang, Z.; Yu, W.; et al. Digital Beamforming Synthetic Aperture Radar (DBSAR): Experiments and Performance Analysis in Support of 16-Channel Airborne X-Band SAR Data. *IEEE Trans. Geosci. Remote Sens.* **2021**, *59*, 6784–6798. [[CrossRef](#)]
- Moreira, A.; Krieger, G.; Hajnsek, I.; Papathanassiou, K.; Younis, M.; Lopez-Dekker, P.; Huber, S.; Villano, M.; Pardini, M.; Eineder, M.; et al. Tandem-L: A Highly Innovative Bistatic SAR Mission for Global Observation of Dynamic Processes on the Earth’s Surface. *IEEE Geosci. Remote Sens. Mag.* **2015**, *3*, 9–23. [[CrossRef](#)]
- Rosen, P.; Hensley, S.; Shaffer, S.; Edelstein, W.; Kim, Y.; Kumar, R.; Misra, T.; Bhan, R.; Sagi, R. The NASA-ISRO SAR (NISAR) mission dual-band radar instrument preliminary design. In Proceedings of the 2017 International Geoscience and Remote Sensing Symposium, Fort Worth, TX, USA, 23–28 July 2017; pp. 23–28.
- De, Y.; Yu, W.; Zhang, H.; Wang, W.; Li, D.; Robert, W.A. Forthcoming spaceborne SAR development. *J. Radars* **2020**, *9*, 1–33.
- Jin, G.; Liu, K.; Liu, D.; Liang, D.; Zhang, H.; Ou, N.; Zhang, Y.; Deng, Y.; Li, C.; Wang, R. An Advanced Phase Synchronization Scheme for LT-1. *IEEE Trans. Geosci. Remote Sens.* **2020**, *58*, 1735–1746. [[CrossRef](#)]
- Xu, Z.; Lu, P.; Cai, Y.; Wu, Y.; Wang, R. Performance Analysis of Channel Imbalance Control and Azimuth Ambiguity Suppression in Azimuth Dual Receiving Antenna Mode of LT-1 Spaceborne SAR System. *Remote Sens.* **2023**, *15*, 2765. [[CrossRef](#)]
- Li, S.Q.; Yang, R.L. Study on Azimuth Signal Processing of Single Phase Center Multiple Beams Synthetic Aperture Radar. *J. Electron. Inf. Technol.* **2005**, *27*, 1073–1076.
- Song, X.; Yu, W. Reconstruct azimuth signal and suppress interbeam ambiguities of SPCMB SAR with Hybrid filterbank. *J. Electron.* **2008**, *25*, 324–329. (In Chinese) [[CrossRef](#)]
- Huber, S.; Younis, M.; Patyuchenko, A.; Krieger, G.; Moreira, A. Spaceborne Reflector SAR Systems with Digital Beamforming. *IEEE Trans. Aerosp. Electron. Syst.* **2012**, *48*, 3473–3493. [[CrossRef](#)]
- Papoulis, A. Generalized sampling expansion. *IEEE Trans. Circuits Syst.* **1977**, *24*, 652–654. [[CrossRef](#)]

30. Zuo, W. Research on High Resolution Wide Swath SAR Imaging Mode and Algorithm. Ph.D. Thesis, University of Electronic Science and Technology of China, Chengdu, China, 2015.
31. Lorenz, R.G.; Boyd, S.P. Robust minimum variance beamforming. *IEEE Trans. Signal Process.* **2005**, *53*, 1684–1696. [[CrossRef](#)]
32. Reed, I.S.; Mallett, J.D.; Brennan, L.E. Rapid convergence rate in adaptive arrays. *IEEE Trans. Aerosp. Electron. Syst.* **1974**, *AES-10*, 853–863. [[CrossRef](#)]

**Disclaimer/Publisher’s Note:** The statements, opinions and data contained in all publications are solely those of the individual author(s) and contributor(s) and not of MDPI and/or the editor(s). MDPI and/or the editor(s) disclaim responsibility for any injury to people or property resulting from any ideas, methods, instructions or products referred to in the content.